Application of CFD on VIM of semi-submersible FOWT: A Case Study

Application of CFD on VIM of semi-submersible FOWT: A Case Study

Fengjian Jiang, Decao Yin, Andrea Califano and Petter Andreas Berthelsen

SINTEF Ocean AS, NO-7050, Trondheim, Norway

fengjian.jiang@sintef.no

Abstract. This study examines the Vortex Induced Motions (VIM) of the INO WINDMOOR 12 MW semi-submersible Floating Offshore Wind Turbine (FOWT) platform using three-dimensional Computational Fluid Dynamics (CFD). The results from both model- and full-scale simulations are presented. The model scale results reveal varying VIM performances at different current headings, with detailed flow visualizations and analyses of hydrodynamic loads on FOWT components providing insights into the underlying wake interaction scenarios. One simulation shows bifurcated VIM, where regular motions are intermittently interrupted due to simultaneous suppression of vortex shedding on all FOWT columns. Preliminary full-scale CFD results suggest a strong scale effect. The paper concludes with a discussion on how CFD simulation can be more effectively used in VIM research.

1. Introduction

Floating offshore wind turbines (FOWTs) are subject to non-linear fluid-structure interaction (FSI) phenomena such as vortex-induced motion (VIM) and galloping during installation, operation, maintenance, and decommissioning. These phenomena can occur due to high towing speeds, strong currents, and environmental loads from waves and winds. VIM and galloping can induce significant drag loads and motions, potentially damaging towing lines, mooring lines, and the turbines themselves. They can also reduce the efficiency of tow-out operations and restrict walk-to-work (W2W) accessibility. As the floating offshore wind industry is still in its early stages, there is a lack of established engineering practices and validated tools or methodologies for addressing these FSI problems. A thorough understanding of the physics of VIM and galloping of FOWTs with typical floaters is crucial for ensuring cost-effective and safe installation, operation, and maintenance of FOWTs.

Small scale model tests in towing tanks are the main methods to investigate the VIM response characteristics. A series of three-column platforms with different cross sections (circular, diamond and square) were tested in [1], with varying relative distance between columns (S/L) and incident angle of the current. It was observed that the effect of the distance between column centers can be neglected when S/L > 3. The current incident angle mainly affected the in-line motion. Similar experiments were performed on the semisubmersible (SS) floating system design developed for the DeepCwind project (Offshore Code Comparison Collaboration Continuation (OC4) phase II) [2]. The experiments covered a wide range of reduced velocities ($3 < V_r < 24$), and Reynolds numbers ($8000 < Re < 70{,}000$). Up to $0.7D$ (where D is the off-column diameter) crossflow VIM response amplitude was observed in the lock-in region $5 < V_r < 10$, while the maximum in-line response amplitude was about $0.2D$.

Computational Fluid Dynamics (CFD) simulations were performed by Liu et al. [3] on the OC4 FOWT (model scale 1:50) [4]. VIM of OC4 subject to current at different incident angles (0°, 90°, 180°) was investigated. It was observed that in-line (IL) motions were much smaller than crossflow (CF) motions. Significant CF response amplitudes (≈0.8D) were observed for all three incident angles at reduced velocity $V_r \approx 8$. Considerable VIM responses were observed over a wide range of reduced velocities, arguing that this phenomenon should be considered in the design phase. For more comprehensive reviews on the topic of VIM, the readers are directed to the review articles [5] and [6].

In this paper, a CFD case study to investigate VIM of a semi-submersible is presented. The floater model and CFD setup are introduced in section 2, followed by verification and validation in section 3. Results and discussions are presented in section 4 and 5, for model scale and full-scale simulations, respectively. Concluding remarks are made in section 6.

2. Theory and numerical setup

2.1. The INO WINDMOOR FOWT model

A new wind turbine concept was designed through the "WINDMOOR" project [7], consisting of the INO WINDMOOR semi-submersible floater [8] and the WINDMOOR 12MW turbine. The INO WINDMOOR semi-submersible floater consists of 3 columns and 3 pontoons that connect the columns.

The 1:40 model, as shown in Figure 1a), was tested in the Ocean Basin of SINTEF Ocean [9]. Right-handed coordinate system is adopted, with X-direction aligned with current pointing towards the tower of the turbine (the corresponding current is referred to as 0° heading), Y-direction as cross flow direction pointing to portside column of the floater, and Z-direction as vertical direction pointing upwards. The main dimensions of the floater (in full scale) are depicted in Figure 1b).

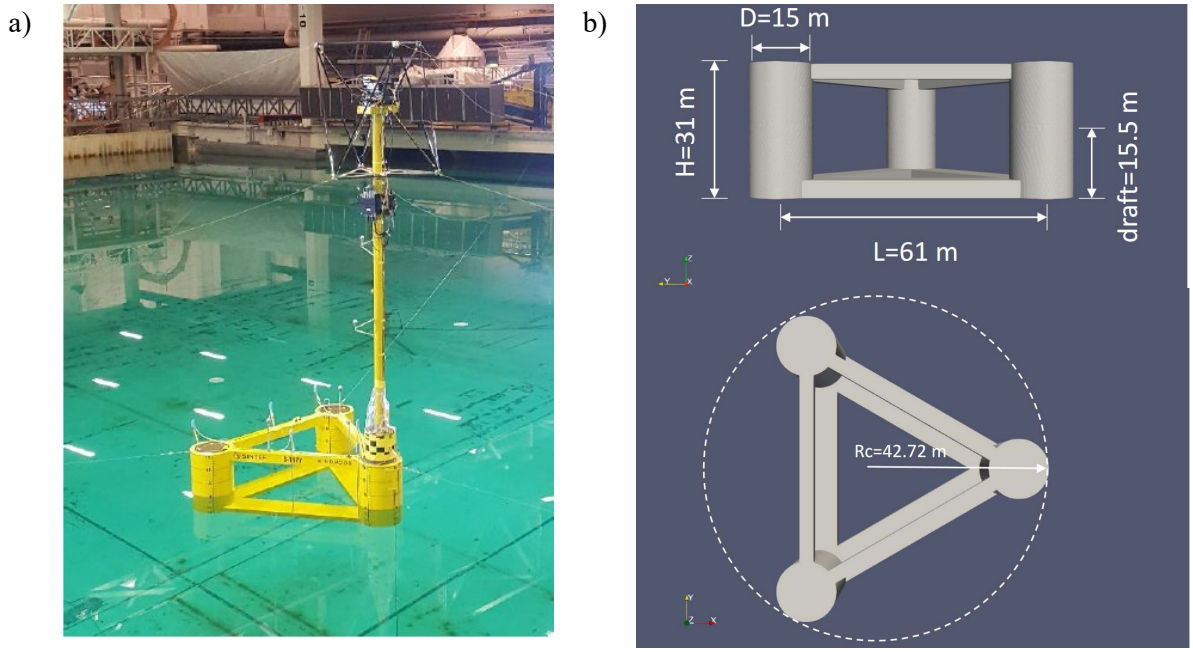

Figure 1. a) The INO WINDMOOR model in SINTEF Ocean's basin (reproduced from [9]). b) Dimensions of the floater.

2.2. Vortex induced motions

VIM is a branch of Vortex-Induced Vibration (VIV), but represented by multi degree-of-freedom (DoF) rigid body motions at high Reynolds numbers (> 10^6). VIM needs to be considered for its considerable motion amplitude, large drag force, and induced high tension force on mooring systems etc. Key quantities in a VIM process are Strouhal number (St) and reduced velocity (V_r). Strouhal

number is a dimensionless number given as the ratio between the predominant frequency of vortex shedding and the diameter of cylinder (D) divided by the free stream velocity:

$$St = f_{St}D/U, \quad (1)$$

where $f_{st} = St\ U/D$ is the vortex shedding frequency of a fixed cylinder in calm water.

The reduced velocity (V_r) is defined as

$$V_r = UT_n/D, \quad (2)$$

where T_n is the still water natural period of the structure in transverse direction.

Motion amplitudes and periods will be used to evaluate VIM performances in this study. Both the maximum- and nominal amplitudes will be discussed, as described in equations (3) and (4).

$$A_i/D_{max} = (S_i^{max} - S_i^{min}) \,/\, 2D \quad (3)$$

$$A_i/D_{norm} = \sqrt{2}\, S_i^{SD} \,/\, D, \quad (4)$$

where A stands for amplitude, S denotes displacements, $i = x, y,$ and the superscript "SD" stands for standard deviation.

Force coefficients are defined as

$$C_{Fi} = F_i/0.5\rho U^2 S_p \quad (5)$$

where ρ is the water density, and S_p is the projected area of the column.

2.3. The CFD setup

The commercial CFD software StarCCM+ was utilized to carry out simulations in this study. The environment is set to calm water with steady current, without waves. Free surface is ignored, due to the small Froude number and thus expected mild free surface effects. The delayed detached eddy simulation (DDES) is selected to model turbulence, which performs as a RANS model in the boundary layers to save computational cost, while resolving directly the large scales of turbulence (LES) in the separation regions to capture more flow details [10] [11] [12].

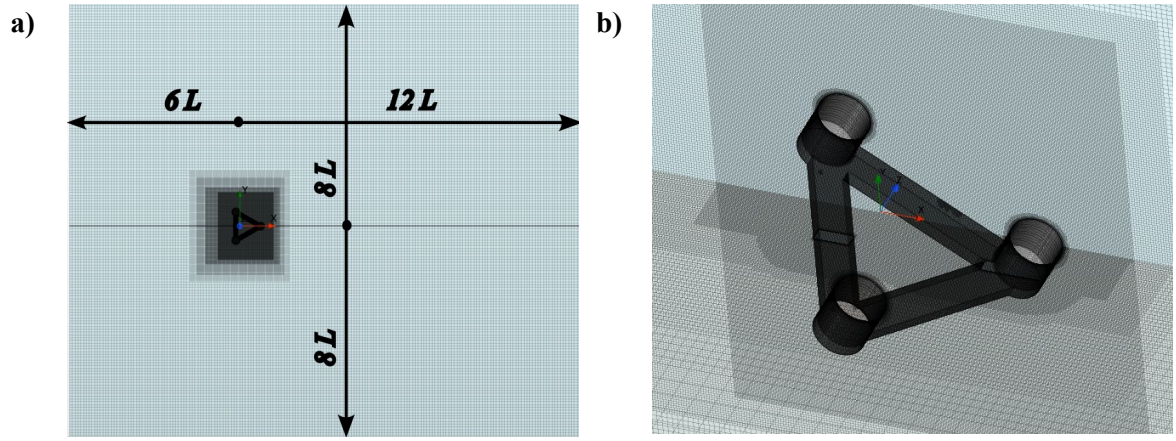

Figure 2. a) Illustration of the computational domain; b) CFD mesh in vicinity of the floater.

In this CFD study, a simplified horizontal mooring system, as designed in a previous model test [9], is used. The horizontal mooring lines are represented as single element mass-spring systems, with equivalent spring stiffness derived from model test measurements. The CFD simulations consider sway and surge as the two degrees of freedom, in line with recent CFD practices for VIM of semi-submersibles [13]. While VIM is inherently a coupled 6-DoF dynamic response, the coupling effects are beyond the scope of this study and will not be discussed further.

Most of the simulations are carried out in model scale (scaling factor 1:40), where the dimensions as depicted in Figure 1b) are scaled down accordingly. The computational domain is rectangular, with a length of 18L in X-direction, where L is the length of the model (Figure 1b), a width of 16L in Y-direction, and a depth that corresponds to 150m water depth in full scale. Figure 2a) gives an impression

of the computational domain in x-y plane. Trimmer meshes with prismatic layers are chosen for the simulations, the trimmer cells are isotropic, and has been specially refined in the vicinity of the floater, in the free shear layer regions and in the wake, to fulfil the requirements of the DDES model. Mesh refinement is applied following multi-level zonal mesh refinement method as a common practice in trimmer meshes. Figure 2b) illustrates the computational mesh close to the floater geometry.

3. Verification and validation

3.1. CFD mesh and time step convergence test

A mesh convergence test was carried out for model scale simulations, three different meshes were considered. The mesh parameters are briefly summarized in Table 1. Note that wall Y+ are kept lower than 5 even for the coarse mesh, as considered appropriate for DES simulations. For the fine mesh, Y+ on the geometry surface is mostly smaller than 1.

In this study, the simulations were firstly run with the geometry fixed, to allow proper development of the flow, then the motion was set free and solved. The simulations ran for at least 20 sway periods after the motion has reached a stable state. A typical sway displacement time history is shown in Figure 3. Sway motions are primarily discussed in this section because, as will be shown later, the motions in surge direction are one order or magnitude smaller compared to those in sway direction.

Table 1. Parameters of the computational meshes for mesh convergence test

Mesh	Reference size / D	Minimum size /D	Total number of cells
Coarse	0.36	0.072	7.0 million
Medium	0.28	0.056	9.4 million
Fine	0.2	0.04	16.0 million

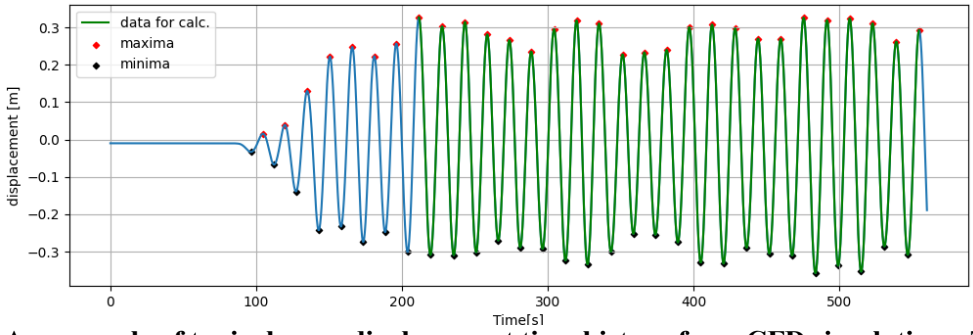

Figure 3. An example of typical sway displacement time history from CFD simulations. The green part marks the data used for VIM amplitude and periods calculations.

The mesh convergence results are plotted in Figure 4a), from which convergence against mesh resolution is seen for A_y/D_{max}, A_y/D_{norm}, and T. Moreover, the differences between results with "medium"- and "fine"-mesh are considerably small to show that the fine mesh has sufficient resolution for the CFD setup in the present study. The fine mesh was henceforth adopted in all following simulations.

With the fine mesh, a time step convergence test was conducted to validate the choice of time step size. Four different time step sizes were chosen: 0.015s, 0.02s, 0.025s and 0.03s, respectively. Results are presented in Figure 4b), showing that independence from the time step size is reached at 0.02s. This value was therefore chosen for the rest simulations in this study.

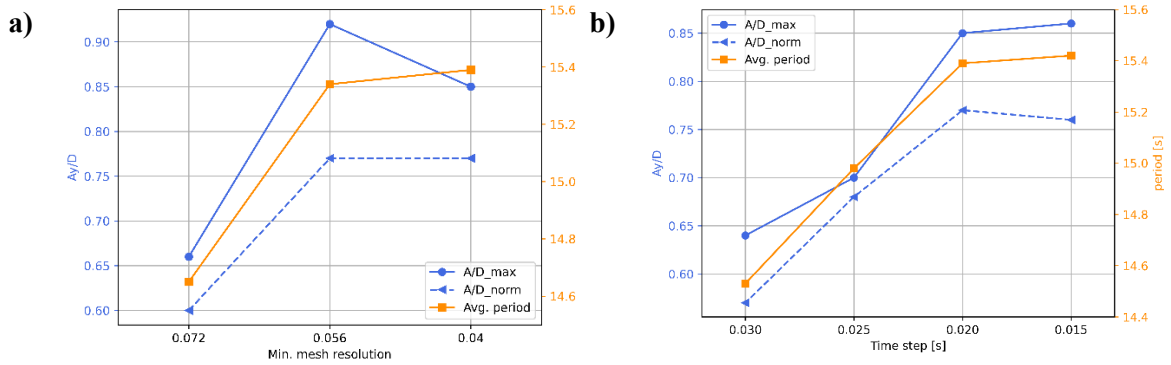

Figure 4. Results of a) mesh convergence test, and b) time step size convergence test

3.2. Validation against model test

There was no VIM test being carried out in the INO WINDMOOR model test, however, the moored sway test is a good candidate for validation purposes. CFD simulations of sway decay test were conducted in both model and full scale, from which the decayed sway motion was monitored and natural frequency T_n of the moored floater were calculated. Detailed comparisons are shown in Table 2. Note that experiments were carried out only in model scale, and full-scale experimental values were scaled accordingly, whereas CFD simulations were carried out in both scales.

Table 2. CFD results of moored sway decay test, compared with experimental results

Scale	$T_{n,CFD}$ [s]	$T_{n,EXP}$ [s]	Deviation
Model Scale	15.02	14.97	0.33%
Full Scale	93.84	94.64	-0.85%

Results in Table 2 show good comparisons between CFD predictions and test measurements, with discrepancies lower than 1% in both model and full scales. This validation shows that the adopted CFD setup can properly solve the forces and corresponding motions of the floater, accurately predicting the overall stiffness and natural frequency of the configuration.

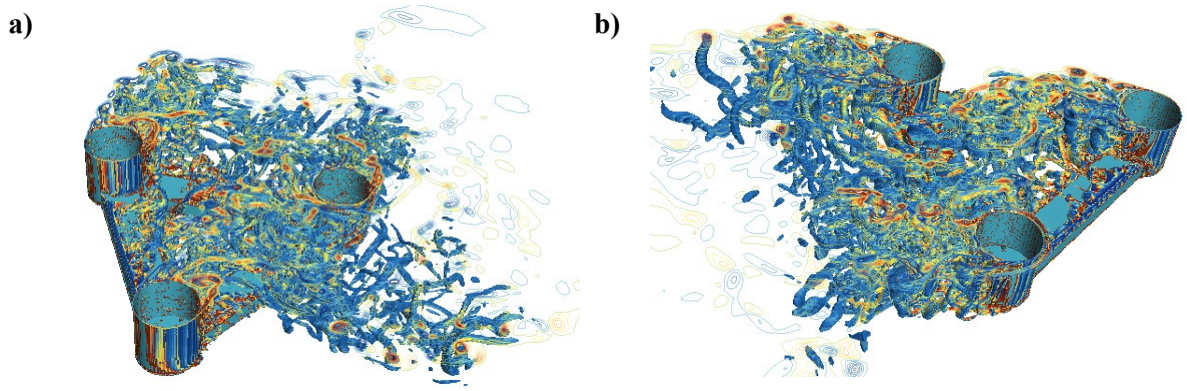

Figure 5. Visualizations of instantaneous wake at a) 0º heading, V_r = 8; and b) 180º heading, V_r = 8. The 3D wake structures are represented by $\boldsymbol{\lambda_2}$ iso-surfaces [14] and colored by vorticity magnitude.

4. Model scale VIM results

Model scale VIM of the INO WINDMOOR semi-submersible floater is primarily investigated under two different current heading angles, 0° and 180°, respectively. The 0° current heading is defined such that two of the three columns are parallel located facing the current while the third column is located downstream, namely, the current is following +*x*-direction as depicted in Figure 2a). The 180° current is reversed, following -*x*-direction. These two headings are selected because they represent distinct wake patterns, as can be intuitively observed from the instantaneous 3D wake visualizations in Figure 5.

4.1. VIM trajectory and VIM design curves

With the surge and sway motion histories from the simulation, it is possible to outline the trajectories of the floater's motion, and further to calculate the VIM curves. Figure 6 illustrates examples of the VIM trajectory at 0° current heading but with two reduced velocities, V_r = 8 and 10. Each sub-figure includes two plots, one on the left showing a zoomed-in view of the trajectory with not scaled surge and sway displacements (data from the last two periods are highlighted in red), and one on the right showing the same trajectory but with surge and sway displacements plotted to-scale.

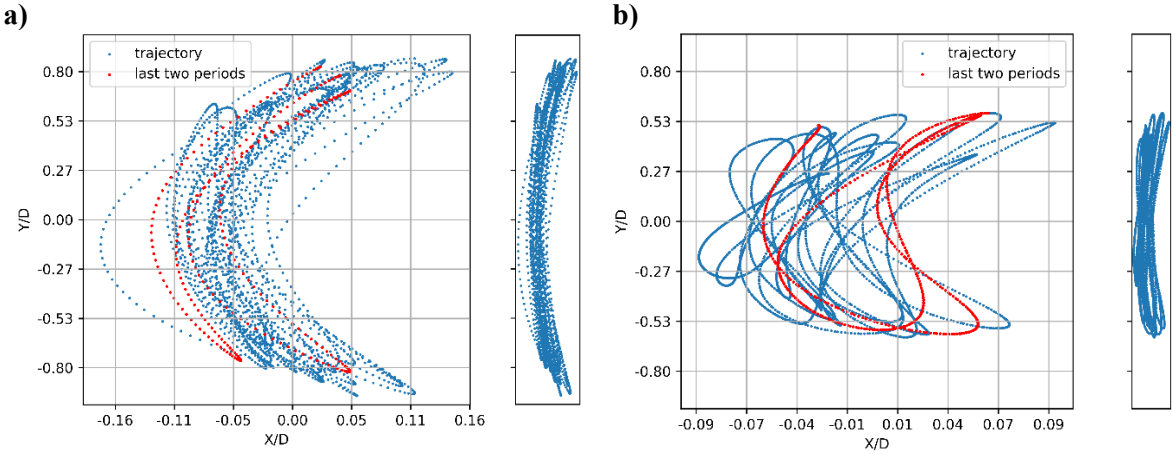

Figure 6. Examples of VIM trajectories from cases: a) 0° heading, V_r = 8; b) 0° heading, V_r = 10.

From Figure 6, it is observed that the VIM trajectories roughly follow an "8" shape, with the middle part of the trajectories slightly skewed. Since the sway motion amplitude is significantly larger than the surge motion amplitude, the former has been the main focus in this study. By comparing the results in Figure 6 a) and b), it is observed that the VIM motion amplitude is larger and more regular at V_r = 8 than that at V_r = 10.

Figure 7 shows the model scale VIM curves measured by sway amplitudes and sway motion periods, respectively. Under both current headings, peak sway amplitude appears at V_r = 8. The shape of the A_y/D curves under different headings are similar, but the curve at 180° heading is clearly flatter, which leads to a much smaller peak A_y/D value as compared to that at 0° heading. The sway motion period, as plotted in Figure 7b), shows a monotonically decreasing tendency as V_r increases, under both current headings. The natural sway period T_n of the whole system is outlined by a dashed red line in Figure 7b), which turns out to be closest to the motion period at V_r = 8, for both current headings. No VIM model test has been carried out, however, the motion period results fall well in the empirical values as summarized in Table 1 in [5].

4.2. Discussions of wake interactions under different current headings

Wake interaction among the three columns is a key aspect to explain the different results at 0° and 180° as observed in Figure 7 (the columns are named as portside, starboard and tower columns, respectively, as marked in Figure 8, the names are kept the same for different headings to ease the discussion). Figure

8 demonstrates the wake interaction effects by showing more detailed results, including force coefficients history (Eq. (5)) and snapshots of the instantaneous wake structures.

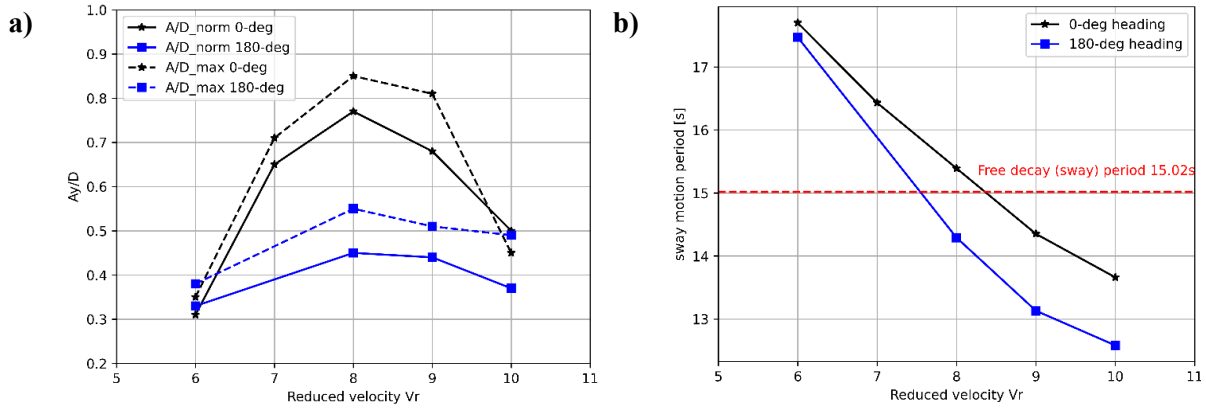

Figure 7. a) The VIM curves measured by both $\boldsymbol{A_y/D_{max}}$ and $\boldsymbol{A_y/D_{norm}}$; b) The sway motion period. Results from 0° and 180° current headings are plotted together in each sub-plot for direct comparisons.

The force histories show very different patterns under the two heading angles. The comparison between Figure 8 a) and e) shows that at 180°, C_{Fx} on the three columns are in average at comparable levels; whereas at 0°, drag force on the tower column is at a significantly lower level as compared to the other two columns. The reason of this, is that at 0°, the tower column is continuously under influence of the wakes from both the upstream portside and starboard columns, as also intuitively seen from the snapshot in Figure 8 c).

Again, looking at Figure 8a), C_{Fx} on the three columns are in general in phase with each other, indicating that the vortex shedding from the two upstream columns are in phase, which also leads to an in-phase shedding from the tower column. However, the scenario is rather different at 180°, *i.e.,* in Figure 8e), where the portside and starboard columns now are downstream in the wake of the otherwise upstream tower column. It is then interesting to see that C_{Fx} on the portside and starboard columns are out-of-phase, and alternatively being in phase with the C_{Fx} of the tower column.

Cross-flow force histories, *i.e.,* C_{Fy}, also turn out to have distinct features at 0° and 180° headings, respectively. Figure 8b) shows that at 0°, C_{Fy} of all three columns are in phase with each other, and at equivalent levels. On the other hand, Figure 8f) shows that C_{Fy} on the portside and starboard columns can be of opposite signs at the same time. For instance, at around t = 330s, C_{Fy} on the portside and tower columns are both positive, while C_{Fy} on the starboard column is negative; at t = 392s, i.e. marked by red vertical lines in Figure 8f), also when the snapshot in Figure 8d) is taken, C_{Fy} on the tower column is close to zero, while C_{Fy} on the portside and starboard columns have again opposite signs.

This could also explain why the sway VIM amplitude at 180° is much smaller as compared to that at 0°, because a certain value of F_y on the portside and starboard columns cancel out due to opposite signs, which further results on a lower total F_y on the overall geometry.

4.3. Bifurcated VIM

In most simulations, the motions are regular, in a similar manner as shown in Figure 3. Yet in one simulation, *i.e.,* $V_r = 10$ at 180° heading, an interesting bifurcated VIM is observed, namely the originally regular vortex induced motions are intermittently interrupted. In Figure 9a), three bifurcated VIM events can be identified in three windows, marked as BF1, BF2 and BF3, respectively. The distinct feature of these events is the abruptly suppressed sway motion amplitude. Figure 9b) and c) show time series of the surge displacement and column drag coefficients, respectively. It is observed that when bifurcated VIM happens, drag forces on the columns are generally at lower levels as compared to when the motions are regular, this consequently leads to obvious surge motions towards +x-direction (in this case the direction where the current comes from).

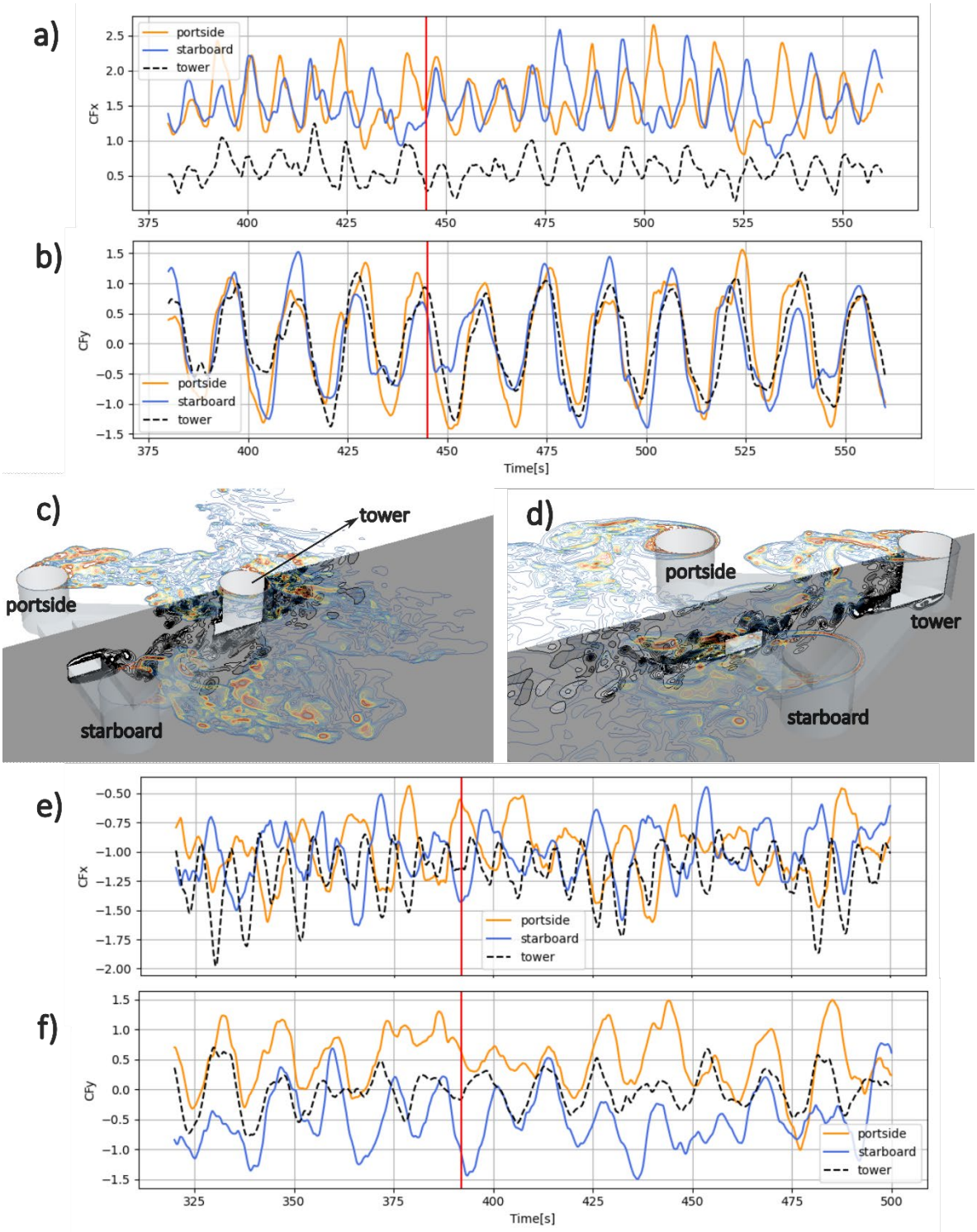

Figure 8. a) and b) are C_{Fx} and C_{Fy} histories of the three columns from the 0° current heading, V_r = 8 simulation. e) and f) are C_{Fx} and C_{Fy} histories of the three columns from the 180° current heading, V_r = 8 simulation. c) and d) are snapshots from 0° and 180° simulations, respectively, represented by vertical vorticity ($\boldsymbol{\omega_z}$) contours in the horizontal plane and cross-flow vorticity ($\boldsymbol{\omega_y}$) contours in the mid-vertical plane. c) is taken at t = 445s, the corresponding time instance is marked by vertical lines in a) and b). d) is taken at t = 392s, the corresponding time instance is marked by vertical lines in e) and f).

A closer look of the instantaneous flow field reveals that during the bifurcated VIM events, vortex shedding from all columns are suppressed simultaneously, thus resulting in small side forces (F_y) and lower drag (F_x). These flow visualization results agree well with force and motion results in Figure 9.

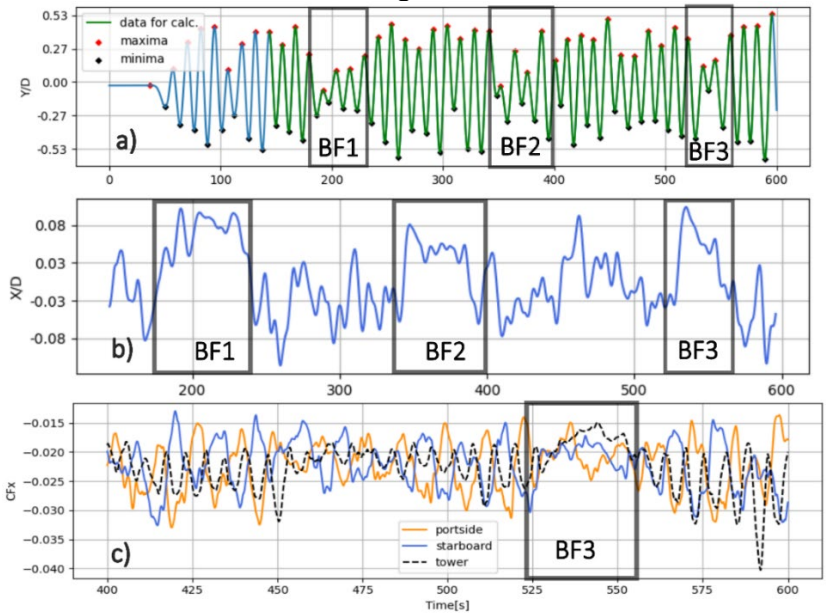

Figure 9. a) Time series of sway displacement (Y/D) in the bifurcated VIM simulation (V_r = 10, 180° heading). b) Time series of surge displacement (X/D). c) Time series of the drag coefficient (C_{Fx}) of the three columns. BF1, BF2 and BF3 mark the three windows where bifurcated VIM happens.

5. Full scale VIM result and scale effect

One full-scale VIM simulation, *i.e.,* V_r = 8 at 0° heading, was conducted in this study. This case was chosen because it has the largest VIM motion in model scale. The computational mesh needs to be specially adjusted for full-scale simulation, which resulted in a mesh that contains 25 million cells, yet this only ensures wall Y+ < 5 on most of the geometry surface. Results in Table 3 show that under the same V_r and heading, full-scale and model scale results are very different. Calculated $\boldsymbol{A_y/D}$ in the full-scale simulation is only slightly larger than 0.1D, significantly lower than those in the model scale simulation. This is a strong indication of scale effects, which root from the conflicts between Froude scaling (which is conventionally used to scale down the geometry and current speed) and Reynolds scaling (which is the main driving mechanism behind the physical process of vortex shedding). With a Froude scaling factor of 1:40, the columns would see a full-scale Re that is more than 250 times larger than the model scale Re, meaning that the flows are already in two completely different regimes.

Table 3 Model scale and full-scale results comparisons

Scale	*Case*	A_y/D_{max}	A_y/D_{norm}
Model Scale	V_r = 8, 0°	0.85	0.77
Full Scale	V_r = 8, 0°	0.14	0.11

The present conclusions are based on the observations from one case only, whereas a generalized conclusion would require further investigations on additional cases varying the input parameters. Nevertheless, the deviations presented in Table 3 are clearly noteworthy.

6. Concluding remarks

VIM of semi-submersible FOWT is a complex FSI problem, involving different aspects such as semi-submersible floater designs, current headings, 6-DOF responses, wave-current interactions, and wake

interactions. Different research tools, each with its special strengths and advantages, are therefore required in order to best understand this problem.

Model tests in basins and/or towing tanks are by far the most recognized and reliable research method for VIM problem, yet there are challenges. For example, the significant cost of large test programs (as intrinsically required by the complexity of VIM itself) and the unavoidable scale effects. Especially in the early design phases, various types of numerical tools can be useful, and CFD is absolutely one alternative.

The work presented in this paper provides a suggestion about how CFD simulations could be applied to obtain a hybrid solution. The use of cost-effective turbulence models (*e.g.*, DDES) helps the screening process and can further reduce the size of the test matrix in test facilities. Furthermore, CFD simulations provide uniquely intuitive visualizations of the otherwise abstract and complex flow field, as well as the possibility of monitoring hydrodynamic forces on flexibly chosen sub-components, improving the understanding of the physical process. Another advantage of CFD is that it can break down complex problems and provide answers to specific questions. For example, as future work of this study, free surface effects and coupling effects among other DoFs can be investigated separately. Lastly, well validated CFD results can fill a database for fully coupled numerical models. Such numerical models based on trustworthy databases are fast, and can handle VIM in complex sea environments efficiently.

References

[1] Gonçalves R T, Chame M E F, Hannes N H, de P. Lopes P P S, Hirabayashi S and Suzuki H 2020 FIM – Flow-Induced Motion of Three-Column Platforms *Int. J. Offshore Polar Eng.* **30(02)** 177–185.

[2] Gonçalves R T, Chame M E F, Silva L S P, Koop A, Hirabayashi S and Suzuki H 2020 Experimental Flow-Induced Motions of a FOWT Semi-Submersible Type (OC4 Phase II Floater) *J. Offshore Mech. Arct. Eng.* **143(1).**

[3] Liu Y, Ge D, Bai X and Li L 2023 A CFD Study of Vortex-Induced Motions of a Semi-Submersible Floating Offshore Wind Turbine *Energies* **16(2)** Art. no. 2

[4] Coulling A, Goupee A J, Robertson A, Jonkman J M and Dagher H 2023 Validation of a FAST semi-submersible floating wind turbine numerical model with DeepCwind test data *J. Renew. Sustain. Ener.*, **5.**

[5] Fujarra A L C, Rosetti G F, de Wilde J and Gonçalves R T 2012 State-of-Art on Vortex-Induced Motion: A comprehensive survey after more than one decade of experimental investigation *Volume 4: Offshore Geotechnics Ronald W. Yeung Honoring Symposium on Offshore and Ship Hydrodynamics ASME 2012 31st International Conference on Ocean, Offshore and Arctic Engineering* pp 561–82

[6] Yin D, Passano E, Jiang F, Lie H, Wu J, Ye N, Sævik S and Leira B J 2022 State-of-the-Art review of Vortex-Induced Motions of floating offshore wind turbine structures *J. Mar. Sci. Eng.* **10** 1021

[7] "WINDMOOR", https://www.sintef.no/projectweb/windmoor/

[8] Souza C, Berthelsen P A, Eliassen L V, Bachynski E E, Engebretsen E and Haslum H 2020 Definition of the INO WINDMOOR 12 MW base case floating wind turbine. *Tech. Rep.* ***OC2020 A-044***, Version 1.3. SINTEF Ocean

[9] Thys M, Souza C, Sauder T, Fonseca N, Berthelsen P A, Engebretsen E and Haslum H 2021 Experimental Investigation of the Coupling Between Aero- and Hydrodynamical Loads On A 12 MW Semi-Submersible Floating Wind Turbine *Volume 9: Ocean Renewable Energy ASME 2021 40th International Conference on Ocean, Offshore and Arctic Engineering* V009T09A030.

[10] Spalart P R, Deck S, Shur M L, Squires K D, Strelets M and Travin A 2006 A New Version of Detached-eddy Simulation, Resistant to Ambiguous Grid Densities *Theoret. Comput. Fluid Dynamics* **20** 181–95

[11] Spalart P R, Jou W-H, Strelets M, Allmaras S R 1997 Comments on the feasibility of LES for wings, and on hybrid RANS/LES approach *Advances in DNS/LES* (ed. Liu C, Liu Z.) Columbus, OH: Greyden Press. pp 137-147

[12] Spalart P R 2009 Detached-Eddy Simulation *Annu. Rev. Fluid Mech.* **41** 181–202

[13] Jang H, Kim D-H, Agrawal M, Loubeyre S, Lee D, Huang J, Law Y Z, Magee A and Koop A 2021 A Joint-Industry Effort to Develop and Verify CFD Modeling Practice for Vortex-Induced Motion of a Deep-Draft Semi-Submersible *Volume 1: Offshore Technology ASME 2021 40th International Conference on Ocean, Offshore and Arctic Engineering.* V001T01A008

[14] Jeong J and Hussain F 1995 On the identification of a vortex *J. Fluid. Mech.* **285** 69–94